Influence of the Combination of Microstructure and Mechanical Fields on Stress Corrosion Cracking Initiation of Cold-Worked Austenitic Stainless Steels

Qi Huang, Y. Charles, Cecilie Duhamel, Monique Gaspérini, Jérôme Crépin

INFLUENCE OF THE COMBINATION OF MICROSTRUCTURE AND MECHANICAL FIELDS ON STRESS CORROSION CRACKING INITIATION OF COLD-WORKED AUSTENITIC STAINLESS STEELS

Qi Huang[1,2], Yann Charles[2], Cécilie Duhamel[1], Monique Gaspérini[2], Jérôme Crépin[1]

[1]*MINES ParisTech, PSL University, MAT - Centre des matériaux, CNRS UMR 7633; 63-65, rue Henri Auguste Desbruères, BP87 91003, Evry, France. Email Address: qi.huang@ mines-paristech.fr.*
[2]*University Paris 13, LSPM - Laboratory of Science of Processes and Materials, CNRS UPR 3407, 99 Avenue Jean Baptiste Clément, 93430, Villetaneuse, France. Email Address: qi.huang@lspm.cnrs.fr.*

This work aims to understand the influence of both microstructure and mechanical fields on stress corrosion cracking (SCC) initiation in cold-worked austenitic stainless steels. To this aim, a SCC test is performed on a 316L stainless steel previously tensile pre-strained at room temperature. The experimental local displacement fields are measured after each loading step, using digital image correlation (DIC) based on microgrids, and from which the strain fields are also derived. In the meantime, a numerical finite element (FE) model is developed with Abaqus, aiming to reproduce the polycrystal features in the microgrid area (grain geometries and orientations). This model is submitted to the DIC-obtained displacement, allowing to simulate the strain and stress fields from polycristalline elastoplasticity constitutive equations. The experimental microstructure, as well as the numerical and experimental mechanical fields obtained at the end of the SCC test is then analyzed, compared and correlated to the cracking network.

I. INTRODUCTION

Low carbon austenitic stainless steels, such as 316L, have been selected as materials in contact with the primary environment of pressurized water reactors (PWR) in nuclear power plants because of their good resistance to uniform corrosion at high temperatures. However, cases of intergranular SCC were reported in cold-worked austenitic stainless steels exposed to PWR primary water[1], leading to a significant research effort invested to better understand the origin of SCC in these alloys[2-8]. In primary water, cold-work was shown to favor SCC initiation and propagation in austenitic stainless steels[6]. In particular, hardness thresholds of 240 $HV_{0.1}$ [Ref.9] and 310 $HV_{0.1}$ [Ref.10] were determined for the first stages of crack initiation and for crack propagation, respectively. Nevertheless, the underlying mechanisms leading to intergranular SCC crack initiation in stainless steels are still not elucidated and need to be further investigated.

Previous works suggest that the grain boundary (GB) character, its inclination with respect to the loading direction[11] as well as strain localization [2, 12-15] and incompatibility at GBs[13] have an effect on SCC initiation.

Therefore, the objective of this work is to investigate the interaction between local mechanical fields, microstructure and cracking network. For this purpose, a coupled experimental/numerical procedure was developed, at the polycrystal scale. Microstructural characterizations by electron backscatter diffraction (EBSD) combined with local displacement and strain fields measurements by digital image correlation (DIC) were performed on a representative elementary surface (RES) of the specimen. The SCC crack distribution obtained at the end of the SCC test was characterized by scanning electron microscopy (SEM). Simultaneously, the strain and stress fields were simulated using a numerical finite element model developed to reproduce the polycrystal features in the RES. The experimental fields and the mechanical fields simulated by finite element calculations were then compared and correlated to SCC cracking network.

II. EXPERIMENTAL PROCEDURE

II.A. Material

The chemical composition of the austenitic stainless steel studied in this work is given in Table I. It is consistent with the French requirements on the design and construction rules for mechanical components of PWR nuclear plants[16] and is therefore representative, in terms of composition, of the 316L stainless steels used in nuclear reactors.

A thermal treatment at 1050°C for 1h in argon atmosphere, followed by oil quenching, is applied to get a recovered and homogeneous microstructure. The microstructure consists of equiaxed austenite grains with an average size of 36±27 μm with no distinct

crystallographic texture, and few percents of residual ferrite bands parallel to the rolling direction[6].

Table I. Chemical composition (in wt %) of the 316L austenitic stainless steel used in this study.

	Cr	Ni	Mo	Mn	Si	P	N	C	S
316L	16.54	10	2.03	1.86	0.62	0.026	0.022	0.016	0.0009
Requirement 316L	16-19	10-14	2.25-2.75	<2	<1	<0.04	<0.06	<0.03	<0.03

Figure 1 shows highly twinned austenite grains (Σ3): twin GBs represent about one half of the GBs. Other CSL (coincidence site lattice) GBs (Σ5 – Σ29) represent about 6% of the GBs.

Of the 43% of general boundaries, 95% are high-angle grain boundaries (HAGB with $\theta \geq 15°$, θ being the disorientation angle) and 5% low-angle grain boundaries (LAGB with $5° < \theta < 15°$).

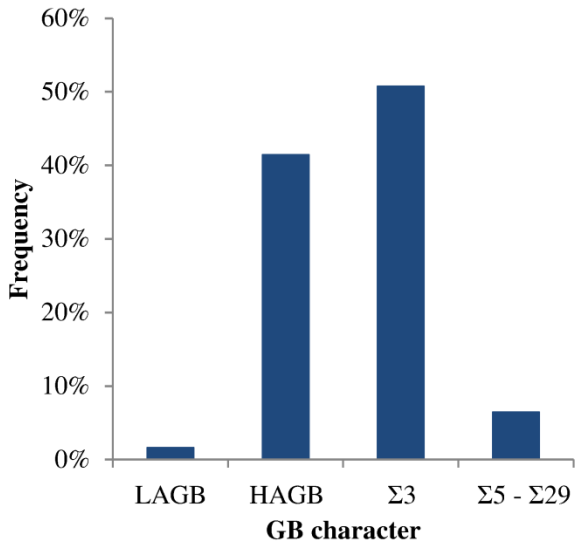

Figure 1. Distribution of the grain boundary character (austenite only).

II.B. Experimental Setup

The geometry of the specimen used for the SCC test is shown in Figure 2. The sample is first pre-deformed at room temperature; then, a slow strain rate tensile test (SSRT) is performed at 340°C in simulated primary water. Figure 3 summarizes the whole procedure. The experimental details for each step will be given in the following.

The specimen surface was grinded down to 1200 grit (~15-20 µm) SiC abrasive paper, followed by diamond paste from 7 µm down to 1 µm. The final mirror polishing was carried out with colloidal silica solution.

Before pre-straining, ten gold-palladium microgrids were deposited using electron micro lithography[9] on one face of the specimen. SEM images of the microgrids were used for DIC analysis to measure the displacement fields. The DIC was performed using the Vic-2D v6 software from Correlated Solutions Inc[17].

The pattern was the same for the ten microgrids: it consisted of a grid with a step of 9.5 µm on which was superimposed a third network of fringes spaced by 12 µm and inclined at 38°. Each microgrid covered a $500 \times 500\ \mu m^2$ area, which was assumed to be a representative elementary surface of the specimen. A mapping of crystal orientations was carried out by EBSD analysis on the areas covered by the microgrids (Figure 4(a)).

The pre-straining step was carried out in air at room temperature and at a strain rate of $5 \times 10^{-4}\ s^{-1}$, up to a strain of 11% for an extensometer with a gauge length 23.4 mm. This value was chosen high enough to favor SCC initiation although low enough to be representative of the cold-worked range expected in-service for the material. SEM images of the microgrids were taken before and after pre-straining for the DIC (n° ⟨1⟩ and ⟨2⟩ in Figure 3).

The SCC test was a SSRT test performed at a strain rate of $1 \times 10^{-8}\ s^{-1}$ up to 4% plastic strain. The tensile axes for the pre-straining and SSRT tests were the same. The SSRT was carried out in nominal primary water in a recirculation loop at 340°C and 165 to 170 bars for a total duration of 905 h. Pure hydrogen at 1.7 bar absolute, 1000 ppm of boron as boric acid and 2 ppm of lithium as lithium hydroxide (LiOH, H_2O) were used to obtain a simulated nominal primary environment.

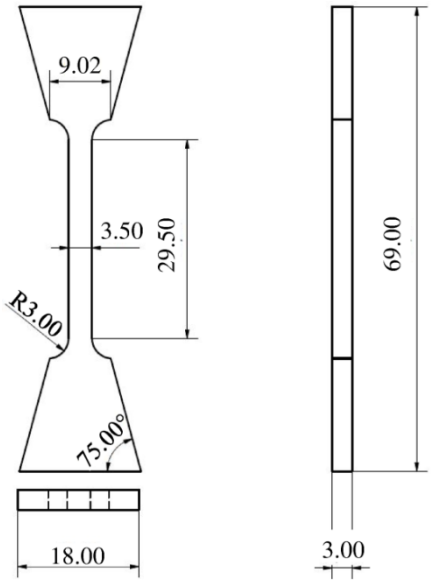

Figure 2. Specimen geometry. The dimensions are given in mm.

During the SCC test, the microgrids features evolved due to both plastic deformation and oxidation. In particular, the formation of a surface oxide layer strongly modified the contrast of the SEM images of the microgrids impeding DIC with a reference image taken before oxidation of the material. To overcome this, a pre-oxidation step was performed between the pre-straining and the SCC steps: the specimen was exposed to the nominal primary water for 150 h at 340°C without being loaded and SEM images of the microgrids were taken after pre-oxidation (n° ⟨3⟩ in Figure 3) and used as reference images for DIC after the SCC tests (n° ⟨4⟩ in Figure 3).

The virtual gauge lengths for pre-straining and SCC DIC were 2.6 µm and 4.6 µm, respectively.

After the SSRT test, the cracking network was characterized by SEM surface observations.

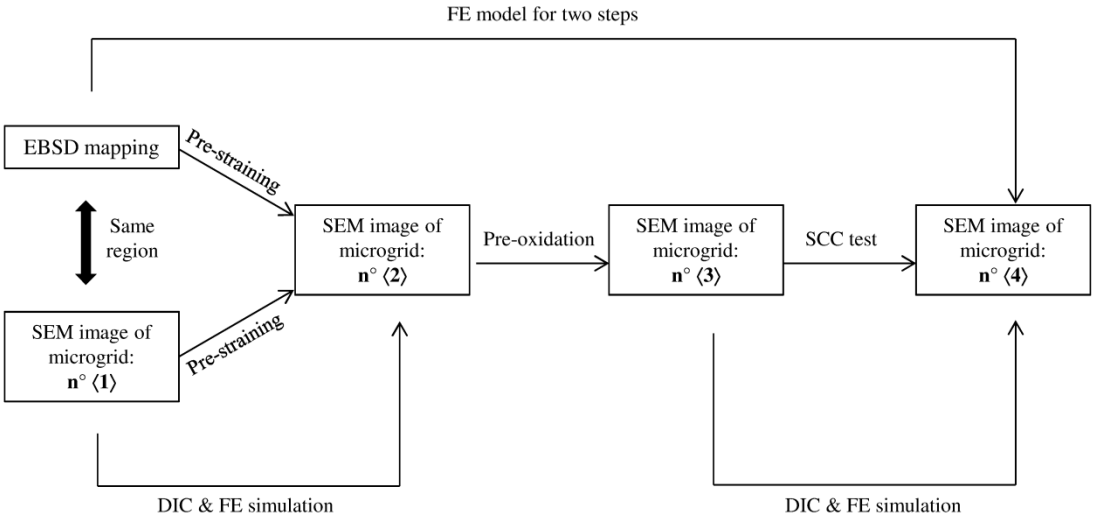

Figure 3. Schematic view of the experimental and numerical procedure.

III. FINITE ELEMENT SIMULATIONS

In order to estimate the mechanical loading experienced by these areas, a numerical model was developed, using Abaqus[18] software and crystal plasticity.

III.A. Geometry and Mesh

Experimental information (results of DIC and EBSD analyses) acquired on the area corresponding to one of the ten microgrids was used as input data for the simulation.

The polycrystalline aggregate was generated from the experimental EBSD crystalline orientation map in Figure 4(a)[19], using OOF2 software[20] for the transposition into finite element mesh, and python scripts to get the 2D geometry associated to that mesh (based on Ref.[21]). This geometry was then extruded (Figure 4(b)) to get a 3D model with a thickness of 12 µm, and meshed.

The aggregate was divided into geometrical grains, which have been meshed with hexahedral trilinear full integration elements, and associated with the experimental orientation obtained from EBSD analyses. In the aggregate, the GB planes were all perpendicular to the surface. The crystallographic orientation of each numerical grain was defined based on the EBSD measurements.

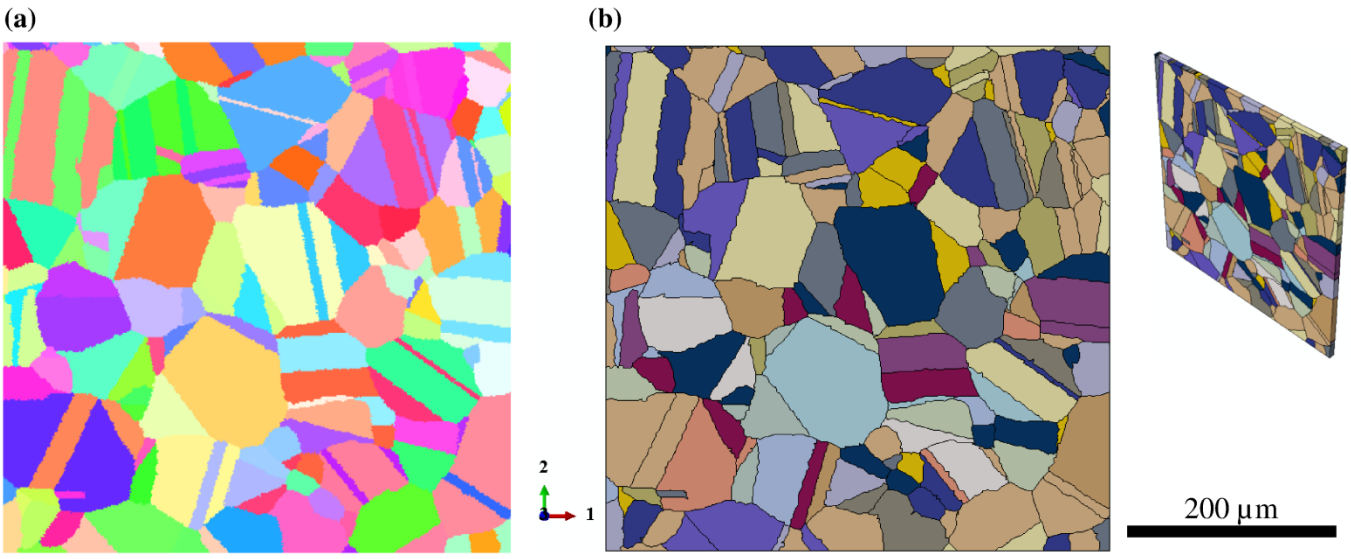

Figure 4 (a) Experimental EBSD mapping and (b) related Abaqus polycrystalline aggregates. The colors on the digital aggregate in (b) are not related to crystalline orientations.

Meshing was carried out with linear hexahedral elements with 8 nodes and complete integration (C3D8 in Abaqus). A total of 216195 elements with a characteristic length of 2 µm was used in this model.

III.B. Constitutive Formulation

Crystal behavior was implemented in Abaqus through a UMAT procedure[18] modified for the purpose of this study, based on the model proposed by Taylor[22], Asaro[23] and Hill and Rice[24].

III.B.1. Mechanical Behaviors

The crystalline plasticity is described by a viscoplastic constitutive law. The sliding rate $\dot{\gamma}^{(\alpha)}$ on the slip system (α) is given by

$$\dot{\gamma}^{(\alpha)}=\dot{a}\ \mathrm{sgn}\left(\tau^{(\alpha)}\right)\left|\frac{\tau^{(\alpha)}}{g^{(\alpha)}}\right|^{n} \qquad (1)$$

where $\dot{a}$ is the reference strain rate on the slip system (α), n the sensitivity coefficient to the strain rate. $\tau^{(\alpha)}$ and $g^{(\alpha)}$ are respectively the resolved and the critical resolved shear stresses on the system. The strain hardening is characterized by the evolution of $g^{(\alpha)}$ through

$$\dot{g}^{(\alpha)}=\sum_{\beta} h_{\alpha\beta}\left|\dot{\gamma}^{(\beta)}\right| \qquad (2)$$

$h_{\alpha\beta}$ represents the self-hardening ($\beta = \alpha$) and latent hardening ($\beta \neq \alpha$) modulus, respectively.

$$\begin{cases} h_{\alpha\alpha}=h_0\ \mathrm{sech}^2\left|\dfrac{h_0\gamma}{g_\infty - g_0}\right| \\ h_{\alpha\beta}=q h_{\alpha\alpha}\ \text{if}\ \beta\neq\alpha. \end{cases} \qquad (3)$$

h_0, g_0 and g_∞ represent the initial hardening modulus, the initial critical resolved shear stress and the maximal critical shear stress, respectively. γ is the cumulative shear strain on all slip systems so that

$$\gamma=\sum_{\alpha}\int_{0}^{t}\left|\dot{\gamma}^{(\alpha)}\right|dt \qquad (4)$$

III.B.2. Identification of parameters

The parameters of the crystalline plasticity constitutive equations were identified using a polycrystalline aggregate made of 200 grains with an average isotropic texture. The polycrystal mechanical behaviors at 20°C and 340°C were identified by comparing the polycrystal average responses with the related experimental tensile curves obtained on the 316L stainless steel (Figure 5) at 20 °C and 340 °C at a strain rate of 1×10^{-3} s^{-1} and 1×10^{-5} s^{-1}, respectively[25]. The identified parameters are given in Table II.

Table II. Parameters in the crystalline plasticity constitutive equations for the pre-straining and SCC steps

T (°C)	E (GPa)	ν	n	$\dot{a}$ (s^{-1})	g_0 (MPa)	g_s (MPa)	h_0 (MPa)	q	$\dot{\varepsilon}$ (s^{-1})
20	193	0.3	50	0.002	98	203	200	1.1	1×10^{-3}
340	170	0.3	50	0.002	65	184	350	1.1	6×10^{-6}

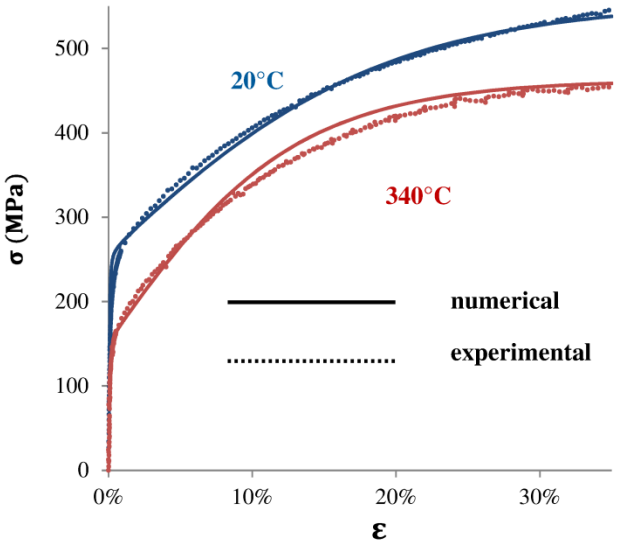

Figure 5. Identification of the parameters for the crystalline plasticity law at 20°C and at 340°C.

Whatever the temperature was, the strain rates used for the parameters identification were not strictly identical to those used experimentally in the present work. However, a good agreement was observed between the mechanical properties at 340°C with a strain rate of 1×10^{-5} s^{-1} in Ref.[25] and a strain rate of 3×10^{-8} s^{-1} in Ref.[26]. Therefore, the effect of the strain rate sensitivity of the material on the overall mechanical behavior was neglected at 340°C and thus the parameters of Table II can be used.

III.C. Boundary Conditions

The boundary conditions applied to the outer contour of the numerical aggregate of Figure 4(b) are the experimental displacement fields obtained by DIC, regularized by continuous functions. As an example, Figure 6(a) illustrates the experimental displacement fields measured along direction 1 after the pre-straining step.

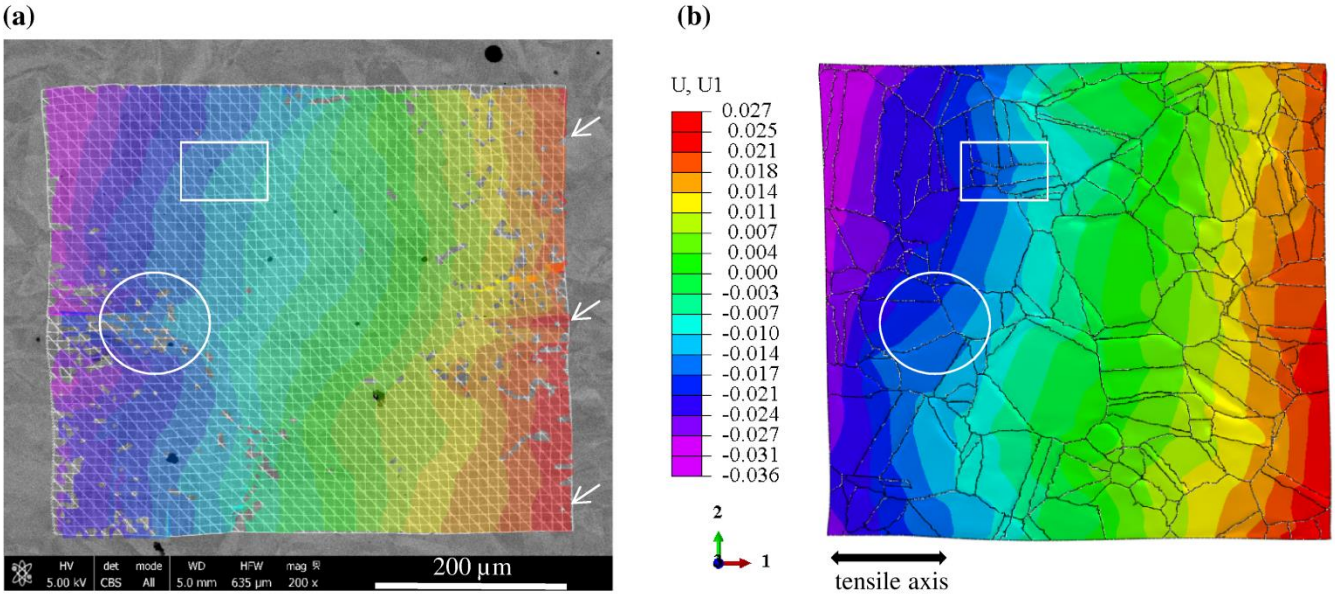

Figure 6. Comparison after the pre-straining step of the (a) experimental and (b) numerical displacement fields along direction 1 (U_1). The units are given in mm.

Figure 7 shows an example of the experimental displacement (obtained by DIC) and the related fit by a continuous function along the tensile direction (direction 1) during pre-straining for the side of the polycrystalline aggregate, indicated by white arrows in Figure 6(a). A close correspondence is observed between the experimental points and the continuous functions while a difference always exits between these two data.

The displacement field is imposed only on the contours of the simulation, leaving the displacements inside the polycrystalline aggregate free.

Points with the same coordinates along 1 and 2 at the outer contour of both the experimental and numerical aggregates have the same displacement regardless of the coordinates along 3.

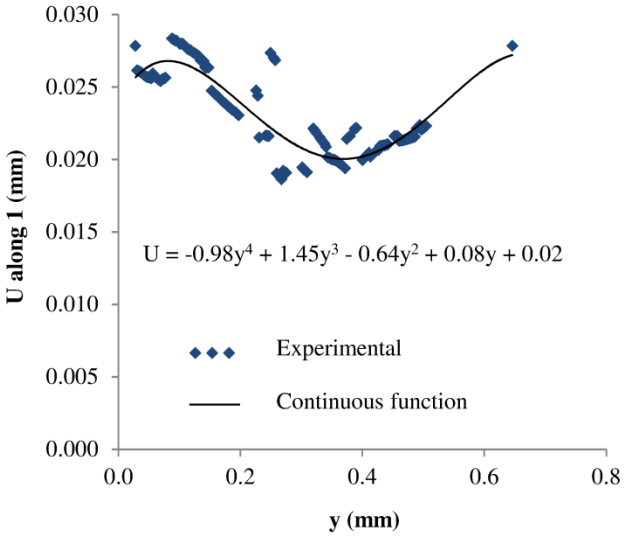

Figure 7. Experimental displacement obtained by DIC and associated continuous function for displacement along direction 1 during pre-straining for one contour.

IV. RESULTS AND DISCUSSIONS

IV.A. Stress Corrosion Cracking Network

The cracking network observed at the end of the SCC test on the area covered by one of the ten microgrids is shown in Figure 8. In total, 28 cracks were counted in this area. All of them are intergranular. These cracks have an average length of 48 µm.

Comparison with the maps of the GB characters reveals that 26 cracks are located at HAGBs. The remaining two cracks are located at Σ5 and Σ27 GBs, respectively. No twin GBs (Σ3) is cracked. The cracked GBs represent 0.12% of the HAGBs, 0.6% of the Σ5 GBs and 0.4% of the Σ27 GBs.

Most cracks are perpendicular to the tensile axis, in agreement with previous results from the literature[11, 15].

A more detailed description of the cracking network obtained on a larger area after the same SCC test is available in Ref. [27].

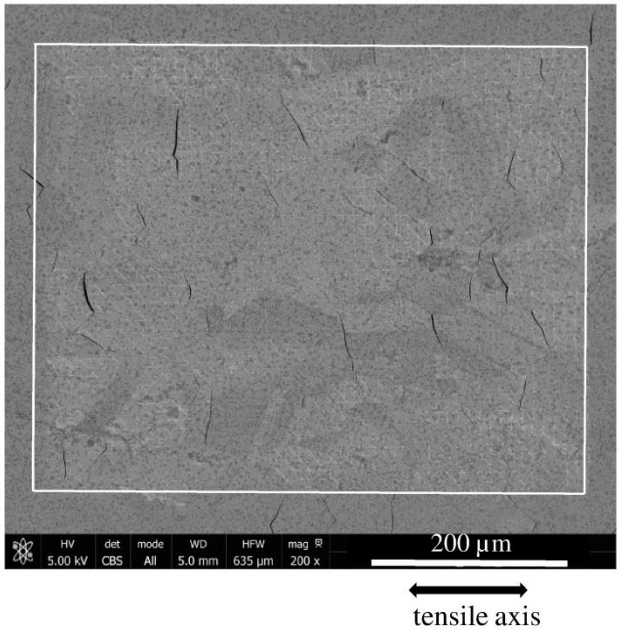

Figure 8. . SCC-induced cracking network in one of the representative elementary surface. The white frame represents the microgrid contour.

IV.B. Mechanical Fields

IV.B.1. Displacement Fields

The displacement field along direction 1 simulated by the FE calculations on the polycrystalline aggregate after pre-straining is illustrated in Figure 6 (b).

The comparison between the experimental and numerical displacement fields shows a good overall agreement both after pre-straining (Figure 6) and after the SCC test.

Few differences are observed, induced by differences between the experimental displacements and the associated continuous functions (Figure 7) and by the different measure bases used for numerical and experimental results: 2 µm for the numerical model and 2.6 µm and 4.7 µm for DIC after pre-straining and SCC test, respectively.

It is also worth underlining that after the SCC test, the real polycrystal presents several cracks, which naturally modifies the displacement repartition by comparison with the numerical procedure, without any cracks. Consequently, the global numerical procedure is considered as validated.

IV.B.2. Strain Fields

The experimental and numerical strain distributions after pre-straining and the SCC test are shown in Figure 9. Only the principal strain along the tensile axis (ε_{11}) is shown in Figure 9.

After pre-straining, the average strain $\varepsilon_{11,\,DIC}$ measured by DIC and the average numerical strain $\varepsilon_{11,\,num}$ are equal to 12% and 10%, respectively. This is consistent with the imposed experimental macroscopic strain (11%).

The strain distributions after the SCC test in Figure 9(b) are obtained considering the displacement fields after the pre-straining step as the reference state (n° ⟨3⟩ in Figure 3). The average strains measured by DIC and calculated by FE simulations are consistent and equal to 2.8% and 2.5%.

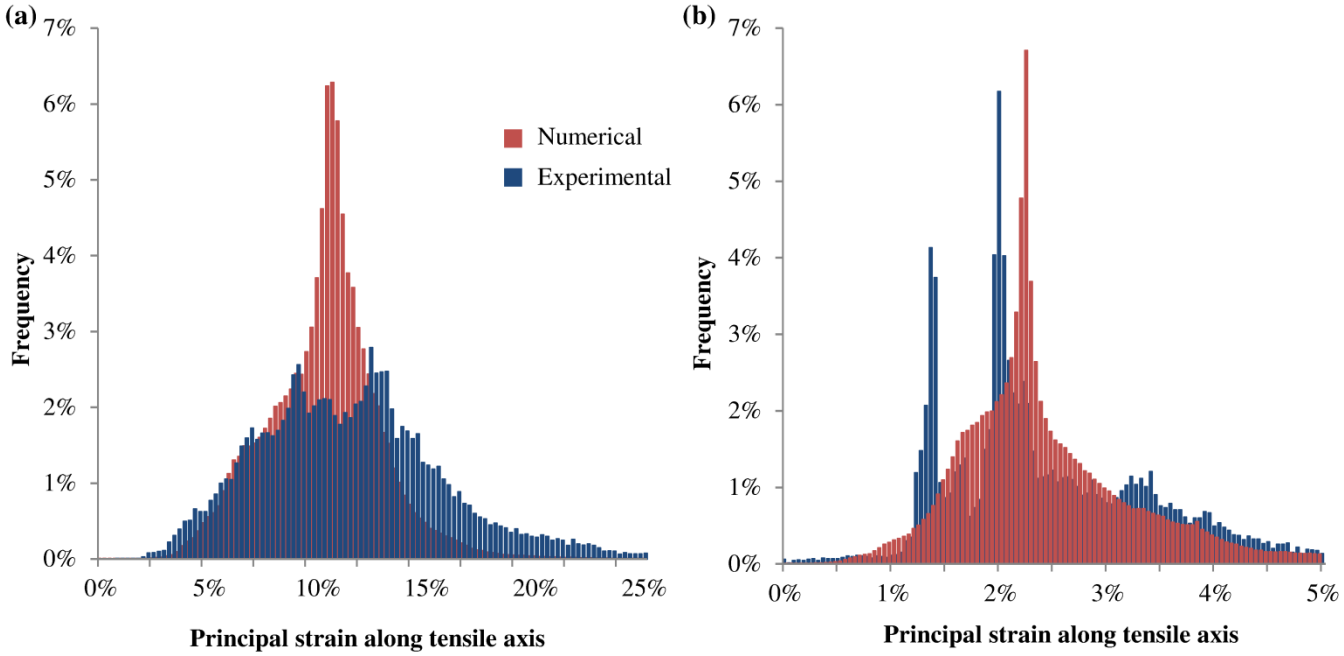

Figure 9. Comparison of the experimental and numerical principal strain histograms along direction 1 ε_{11} (a) after the pre-straining and (b) after the SCC test.

According to Figure 9, the distributions of the numerical strains are narrower than the experimental distribution both after pre-straining and the SCC test. Several sources may explain this difference. The different measurement base between experimental and numerical steps can have an influence: the experimental measurement bases are always higher to numerical ones. The difference between the experimental displacement at the four outer contours and the continuous functions imposed in the FE model (Figure 7) can also affect the calculated displacement, and then the strain field. Some differences are found in the numerical and experimental displacement fields, for example, in the regions in the white oval and rectangle. The difference in the displacement fields will also introduce strain difference. In addition, the constitutive equations used in the FE simulations cannot take into account all information about the experimental crystalline plasticity, also leading to different strain histograms.

Lastly, cracks initiation and opening during the SCC test generate displacements that are taken into account in the experimental strain fields but not in the simulated ones. Therefore, the presence of these cracks also partially explains the differences in the shape of the two strain distributions obtained after the SCC test.

Figure 10(a) represents the maximal principal strain (LEMax) field after the SCC test simulated by the FE calculations and which integrates the whole mechanical history of the specimen (i.e. deformation between steps n° ⟨1⟩ and n° ⟨4⟩ in Figure 3). Figure 10(a) shows that the strain is homogeneous within the unit grain while strain localization is observed in the vicinity of some GBs.

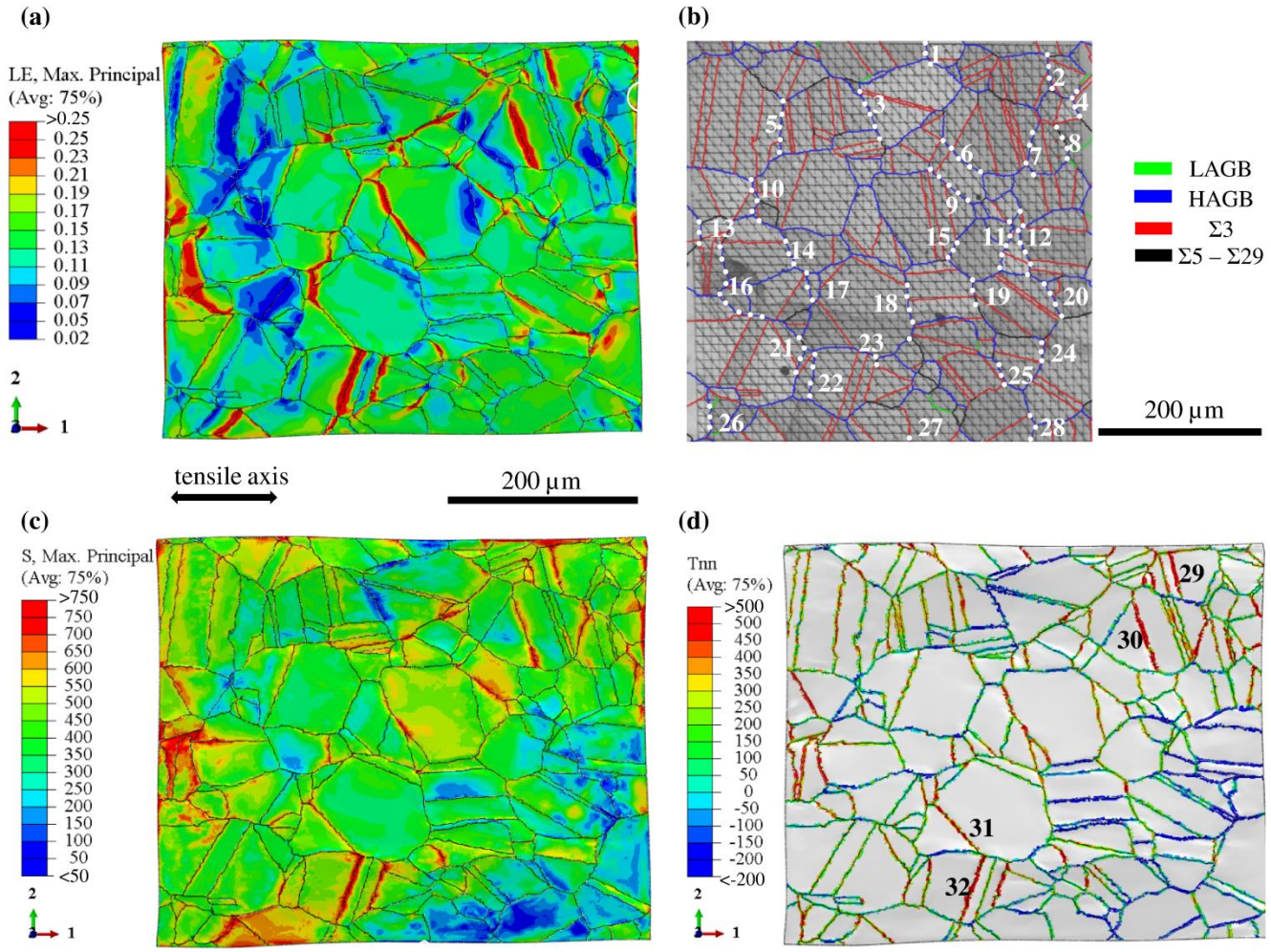

Figure 10. (a) Numerical maximal principal strain (LEMax) fields after the SCC test, (b) grain boundary character mapping (EBSD); the cracks observed at the end of the SCC test are indicated by white dashed lines, (c) numerical maximal principal stress (SMax) fields after SCC test, (d) numerical grain boundary normal stress (T_{nn}) fields after SCC test. The stresses are given in MPa.

IV.B.3. Stress Fields

After the pre-straining step, the experimentally measured macroscopic stress is equal to 431 MPa while the average numerical Von Mises stress in the polycrystal is 462 MPa (i.e. a relative difference of 7%). This difference may be induced by the slight discrepancy observed in Figure 5 between the experimental and numerical mechanical tensile curves in the 10% - 20% strain range and resulting from the parameters identification of the crystalline plasticity law at 340°C. The difference may also result from the FE model used in the simulation: the crystal plasticity in the 316L used in this study may not be described accurately by the numerical constitutive laws used.

After the SSRT test, the experimentally measured macroscopic stress is equal to 410 MPa. The resulting maximal principal stress field and the grain boundary normal stress field T_{nn} are shown in Figure 10(c) and (d). The normal stress is the projection of the stress on the direction normal to the GB plane and computed from Abaqus outputs using a python script. The stress fields in Figure 10 are calculated at the end of the SCC test while the specimen is still loaded and integrate the residual stresses generated during the pre-straining step.

The statistical T_{nn} distribution is shown in Figure 11(a) and exhibits a wide dispersion between -600 and 800 MPa, with an average stress of 138 MPa. In terms of length, 15% of the GBs sustain a T_{nn} stress higher than 410 MPa (experimental macroscopic stress).

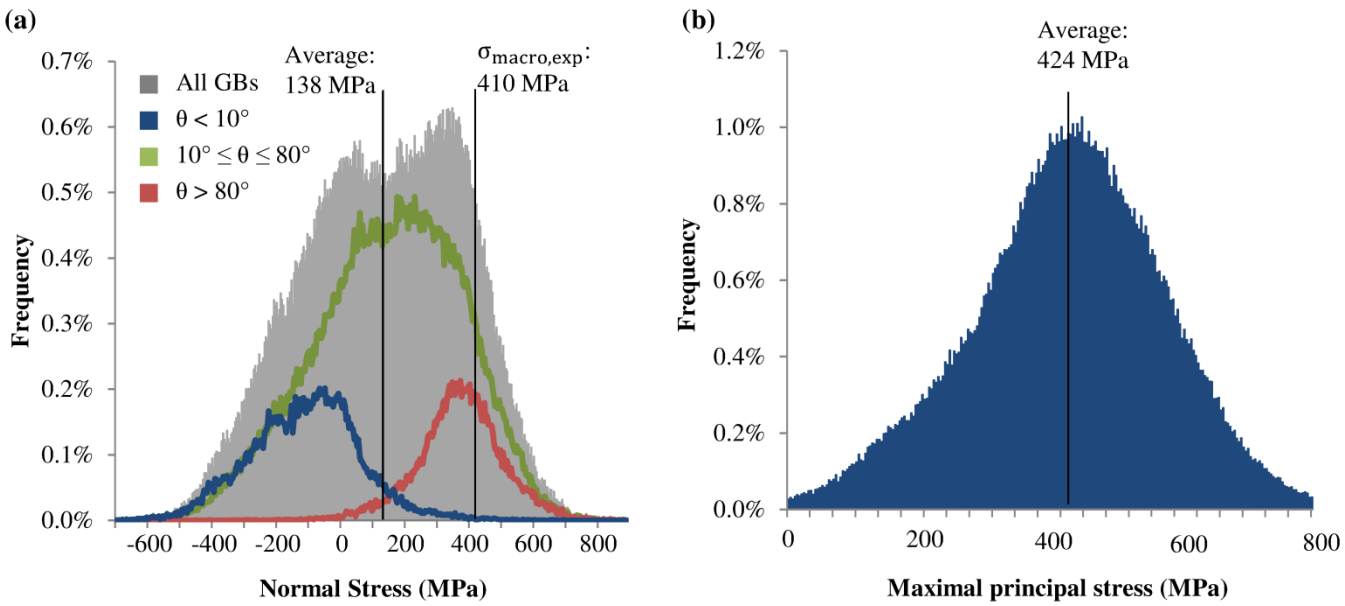

Figure 11. Distribution of (a) normal stress (T_{nn}) along grain boundaries and (b) maximal principal stress (SMax) after SCC test.

The statistical distribution of the maximal principal stress is shown in Figure 11(b). The stress values are all positive and range between 0 MPa and 800 MPa, with an average value of 424 MPa.

As most of the cracks initiate at GBs perpendicular to the tensile axis (Figure 8), the GBs are separated into three groups that differ by their trace inclination θ with respect to the tensile axis: 14% of the GBs are perpendicular to the tensile axis ($\theta > 80°$), 18% of them are parallel to the tensile axis ($\theta < 10°$) and the remaining GBs have an inclination ranging between 10° and 80°.[a] The normal stress T_{nn} distribution for each group of GBs is given in Figure 11(a).

The distribution of the normal stresses applying to the GBs perpendicular to the tensile axis ($\theta > 80°$) is shifted towards the highest values. For this population of GBs, the normal stress is always positive, ranging from 0 MPa to 720 MPa (for a macroscopic experimental stress of 410 MPa). These GBs are among those exhibiting the highest local normal stresses and thus are more prone to failure risks.

On the contrary, the distribution of the normal stresses applying to the GBs parallel to the loading direction ($\theta < 10°$) is shifted towards the lowest values with 73% of stress values in the negative range in terms of length. As a consequence, they present a lower failure risks.

In terms of length, the distribution for the last population of GBs ($10° \leq \theta \leq 80$) has 25% of the stress values in the negative range. These GBs thus exhibit a failure risk in between the two other groups.

[a] The percentages are in terms of GB length.

IV.C. Correlation between the Microstructural and Mechanical Fields and the Cracking Network

Figure 10(b) illustrates all the cracked GBs, numbered from C1 to C28 and Table III summarizes the maximal normal stress (T_{nn}), maximal principal stress (SMax), angle between the GB and tensile axis (θ) and the GB character for each of them. Most of the cracked GBs are HAGB.

When one crack propagates, at the surface, along several GBs, every θ is listed. Compared with Figure 8, 19 of these 28 cracks exhibit one of these two configurations: the crack is perpendicular to the tensile axis ($\theta > 80°$) or at least one GB is perpendicular ($\theta > 80°$) to tensile axis when a crack concerns several GBs. None of the GB parallel to tensile axis ($\theta < 10°$) is cracked.

According to Figure 10(a), the average LEMax for every crack has an average of 14%. However, not all the HAGBs that sustain a LEMax value in this range are cracked as evidenced by Figure 10 (b).

Figure 12 shows the distribution of the maximal value of T_{nn} along the cracked GBs with an average of 504 MPa. Table III and Figure 12 show that 20 among the 28 cracked GBs sustain a normal stress value higher than the 410 MPa, i.e. the macroscopic stress applied during the SCC test. However not all the HAGBs that sustained a normal stress in this range are cracked as evidenced by Figure 10 (b) and (d). On the contrary, 8 GBs fail while the normal stress applying on them is lower than the macroscopic stress.

Table III. Maximal T_{nn} along GB, maximal SMax, θ and GB character for the cracks indicated in Figure 10. The cracks are ordered by decreasing values of the normal stress.

	T_{nn} max (MPa)	SMax max (MPa)	θ	GB character			T_{nn} max (MPa)	SMax max (MPa)	θ	GB character
C23	769	838	89°	Σ5		C26	539	641	90°	HAGB
C16	756	864	82°, 52°, 32°	HAGB		C2	528	666	88°	HAGB
C9	700	805	90°, 45°	HAGB		C5	491	542	86°	HAGB
C4	680	822	80°, 66°	HAGB		C15	483	621	72°	HAGB
C7	665	715	81°, 45°	HAGB		C11	482	532	76°, 60°	HAGB
C22	664	716	87°	HAGB		C10	475	515	77°, 72°	HAGB
C13	662	843	89°	HAGB		C14	372	507	73°	HAGB
C17	638	643	85°	HAGB		C28	348	380	90°, 75°	HAGB
C6	586	606	45°	HAGB		C12	325	452	90°, 72°	HAGB
C8	579	725	90°, 65°	Σ27		C1	319	459	88°	HAGB
C24	571	606	82°	HAGB		C27	275	375	90°	HAGB
C21	553	612	76°, 67°	HAGB		C20	223	379	66°	HAGB
C18	549	658	80°	HAGB		C25	219	435	62°	HAGB
C19	540	544	85°	HAGB		C3	119	313	72°	HAGB

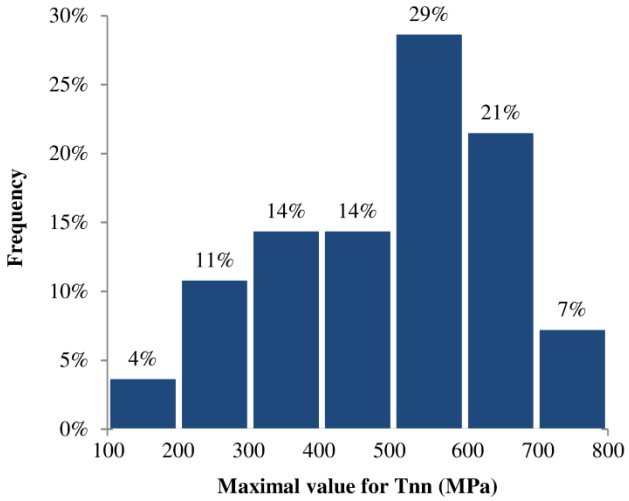

Figure 12. Distribution of the maximal normal stress (T_{nn}) applying to cracked GBs.

These results show that the sole influence of the mechanical fields is not sufficient to account for SCC initiation. Indeed, GBs perpendicular to the tensile axis and that exhibit both a high deformation in their vicinity and a high normal stress don't crack (e.g. R29-R32). These GBs are twin boundaries, suggesting that the GB character plays a great role in SCC initiation, in agreement with previous results from the literatures [11, 15, 28]. On the contrary, cracks may initiate even at GBs that are not heavily loaded. These results suggest that intergranular oxidation also has to be considered in a SCC fracture criterion as the intergranular oxide most probably weakens the GBs, leading to lower stresses necessary to initiate SCC[29, 30].

V. CONCLUSIONS

An approach consisting of coupling experiments and finite element simulations was developed in order to investigate the influence of the combination of microstructure and mechanical fields on SCC initiation of cold-worked 316L stainless steel. After a slow strain rate test in primary water at 340°C, intergranular SCC cracks were observed. They are mostly located at high-angle GBs.

The experimental strain fields measured by DIC and the simulated stress fields calculated by FE simulations show that both the deformation and the stress are homogeneous within unit grains, at the scale considered in this work. Strain and stress concentrations are observed in the vicinity of some GBs, among which are twin boundaries (Σ3). However, these GBs are not cracked.

Cracked GBs are mostly perpendicular to the tensile axis and the maximal normal stress that applies on the GB plane is mostly situated at the range of 504 ± 200 MPa. However, not all the HAGBs that sustain such a normal stress crack, suggesting that the normal stress is not a sufficient criterion to account for SCC initiation.

In particular, the intergranular oxidation depth has to be considered. Further work will consist in coupling the numerical mechanical model reported here with an intergranular diffusion/oxidation model of the GBs in order to better describe the GB failure.

ACKNOWLEDGMENTS

Catherine Guerre (CEA) and Marc Maisonneuve (CEA / MINES ParisTech) are gratefully acknowledged for the SCC test.

REFERENCES

[1] T. COUVANT *et al.*, "PWSCC of austenitic stainless steels of heaters of pressurizers," *5th International Symposium on Contribution of Marerials Investigations to improve the Safety and Performance of LWRs (Fontevraud 5)*, Paper A100 (2006).

[2] W. KARLSEN, G. DIEGO, and B. DEVRIENT, "Localized deformation as a key precursor to initiation of intergranular stress corrosion cracking of austenitic stainless steels employed in nuclear power plants," *J. Nucl. Mater.*, **406**, 138 (2010).

[3] J. CHEN *et al.*, "The effects of cold rolling orientation and water chemistry on stress corrosion cracking behavior of 316L stainless steel in simulated PWR water environments," *J. Nucl. Mater.*, **472**, 1 (2016).

[4] L. ZHANG and J. WANG, "Effect of dissolved oxygen content on stress corrosion cracking of a cold worked 316L stainless steel in simulated pressurized water reactor primary water environment," *J. Nucl. Mater.*, **446**, 15 (2014).

[5] K. ARIOKA, T. YAMADA, T. TERACHI, and T. MIYAMOTO, "Dependence of Stress Corrosion Cracking for Cold-Worked Stainless Steel on Temperature and Potential, and Role of Diffusion of Vacancies at Crack Tips," *CORROSION*, **64**, 691 (2008).

[6] P. HUGUENIN, J. CREPIN, C. DUHAMEL, H. PROUDHON, and F. VAILLANT, "Initiation of stress corrosion cracking in pre-strained austenitic stainless steel exposed to primary water," *Proceedings of the 16th International Conference on Environmental Degradation of Materials in Nuclear Power Systems — Water Reactors* (2013).

[7] L. CHANG, M. G. BURKE, and F. SCENINI, "Stress corrosion crack initiation in machined type 316L austenitic stainless steel in simulated pressurized water reactor primary water," *Corros. Sci.*, **138**, 54 (2018).

[8] T. SHOJI, Z. LU, and Q. PENG, "6 - Factors affecting stress corrosion cracking (SCC) and fundamental mechanistic understanding of stainless steels," in *Stress Corrosion Cracking*, V. S. Raja and T. Shoji, Eds. Woodhead Publishing, pp. 245–272 (2011).

[9] T. COUVANT, L. LEGRAS, F. VAILLANT, J.-M. BOURSIER, and Y. ROUILLON, "Effect of strain-hardening on stress corrosion cracking of AISI 304L stainless steel in PWR primary environment at 360℃," *Proceedings of the 12th International Conference on Environmental Degradation of Materials in Nuclear Power Systems — Water Reactors*, pp. 1069–1079 (2005).

[10] L. TRIBOUILLOY, F. VAILLANT, J.-M. OLIVE, and M. PUIGGALI, "SCC of cold-worked austenitic stainless steels in PWR environment," *Proceeding of the 13th International Conference on Environmental Degradation of Materials in Nuclear Power System - Water Reactors.*, pp. 937–952 (2007).

[11] M. LE MILLIER *et al.*, "Irradiation assisted stress corrosion cracking of stainless steels in a PWR environment (A combined approach)," *Proceedings of the 15th International Conference on Environmental Degradation of Materials in Nuclear Power Systems — Water Reactors*, pp. 1293–1307 (2016).

[12] EPRI, Palo Alto, CA, and EDF R&D, "Understanding the Interaction Between Localized Deformation in Materials and Environmentally Assisted Cracking," Moret sur Loing (2006).

[13] S. NOURAEI, D. TICE, D. M. WRIGHT, and J. Q. da FONSECA, "Towards a mechanistic understanding of the influence of thermo-mechanical treatment on crack initiation in high temperature PWR environments," *Proceedings of the 16th International Conference on Environmental Degradation of Materials in Nuclear Power Systems — Water Reactors* (2013).

[14] T. COUVANT, L. LEGRAS, C. POKOR, F. VAILLANT, Y. BRECHET, and J.-M. BOURSIER, "Investigations on the mechanisms of PWSCC of strain hardened austenitic stainless steels," *Proceeding of the 13th International Conference on Environmental Degradation of Materials in Nuclear Power System - Water Reactors* (2007).

[15] E. A. WEST and G. S. WAS, “A model for the normal stress dependence of intergranular cracking of irradiated 316L stainless steel in supercritical water,” *J. Nucl. Mater.*, **408**, 142 (2011).
[16] ROLLINGBOX, “Code RCC-M AFCEN – Matériels Mécaniques des îlots nucléaires REP,” *AFCEN*. [Online]. Available: https://afcen.com.
[17] “Correlated Solutions – VIC-2D.”. [Online]. Available: https://www.correlatedsolutions.com/vic-2d/
[18] Y. HUANG, “A User-Material Subroutine Incorporating Single Crystal Plasticity in the ABAQUS Finite Element Program,” *Mech Rep.*, **178** (1991).
[19] A. C. E. REID, R. C. LUA, R. E. GARCIA, V. R. COFFMAN, and S. A. LANGER, “Modelling Microstructures with OOF2,” *Int. J. Mater. Prod. Technol.*, **35**, 361 (2009).
[20] “OOF2.” [Online]. Available: https://www.ctcms.nist.gov/oof/oof2/.
[21] “python script for abaqus to create geometry from 3D Orphan mesh.” [Online]. Available: https://www.tugraz.at/fileadmin/user_upload/Institute/IWB/Lehre/Software/ABAQUS/abq3Dmesh2geom.py.
[22] G. I. TAYLOR, “Plastic strain in metals,” *J Inst Met.*, **62**, 307 (1938).
[23] R. J. ASARO, “Crystal Plasticity,” *J. Appl. Mech.*, **50**, 921 (1983).
[24] R. HILL and J. R. RICE, “Constitutive analysis of elastic-plastic crystals at arbitrary strain,” *J. Mech. Phys. Solids*, **20**, 401 (1972).
[25] Q. Huang, Y. Charles, C. Duhamel, M. Gasperini, and J. Crepin, “Mechanical Fields on Cross-Shaped Specimens for Stress Corrosion Cracking of Cold-Worked Austenitic Stainless Steels,” *Materials Science Forum* (2018).
[26] T. COUVANT, F. VAILLANT, J.-M. BOURSIER, and D. DELAFOSSE, “Effect of strain-path on stress corrosion cracking of AISI 304L stainless steel in PWR primary environment at 360 ° C,” *Eurocorr 2004*, Nice, France (2004).
[27] M. MAISONNEUVE, C. DUHAMEL, C. GUERRE, J. CREPIN, and I. de CURIERES, “Effect of oxygenated transients on oxidation and SCC of predeformed stainless steels in PWR primary water,” *Proceedings of the 19th International Conference on Environmental Degradation of Materials in Nuclear Power Systems — Water Reactors* (2019).
[28] V. Y. GERTSMAN and S. M. BRUEMMER, “Study of grain boundary character along intergranular stress corrosion crack paths in austenitic alloys,” *Acta Mater.*, **49**, 1589 (2001).
[29] K. KRUSKA *et al.*, “Atom-probe tomography of surface oxides and oxidized grain boundaries in alloys from nuclear reactors,” *MRS Online Proc. Libr. Arch.*, **1514**, 107 (2013).
[30] A. HERBELIN, T. COUVANT, L. LEGRAS, D. DELAFOSSE, and G. ILBEVARE, “Oxidation of austenitic stainless steels in PWR primary water,” *European Corrosion Congress 2009 (EUROCORR 2009)*, **3**, pp. 1592–1608 (2010).